

CHARACTERIZING THE VARIABILITY OF BLACK HOLE ACCRETION FLOWS
IN GRMHD SIMULATIONS

By

ROHIN SANT

A Thesis Submitted to The W.A. Franke Honors College

In Partial Fulfillment of the bachelor's degree
With Honors in

Physics

THE UNIVERSITY OF ARIZONA

DECEMBER 2025

Approved by:

Faculty Thesis Mentor's Name:

Faculty Thesis Mentor's Department:

Characterizing the Variability of Black Hole Accretion Flows in GRMHD Simulations

ROHIN SANT,¹ BORIS GEORGIEV,¹ AND CHI-KWAN CHAN¹

¹*Steward Observatory and Department of Astronomy, University of Arizona, 933 N. Cherry Ave., Tucson, AZ 85721, USA*

ABSTRACT

Studying variability in black hole environments gives insights on high energy plasma physics, gravity and accretion. Recently, a statistical analysis has been enabled through observational efforts such as the Event Horizon Telescope (EHT) and the computational feasibility of General Relativistic Magnetohydrodynamic (GRMHD) simulations. In this study, we investigate the morphology and evolution of spiral-like variability structures that emerge naturally in these simulations and we present a functional form for analyzing these features directly in the image domain. We measure the shape, sizes, and pitch angles of the spiral features, and investigate how these structures move and diffuse across the spatiotemporal image domain. Our analysis reveals that the pitch angle exhibits a distinct kink that may indicate transitions in the flow dynamics. We also find evidence of a population of spiral arms with different pitch angles. We measure the spiral arms are rotating outward at around 0.03 radians per GM/c^3 . This parameterized variability model provides a new approach to characterizing variability features in GRMHD simulations. Moreover, it offers a potential pathway to refining existing Gaussian Random Field models used in EHT analyses by enabling and enhancing the subtraction of structured variability from both simulated and observational data. This model will also be useful to analyze variability structures in the upcoming movie campaign conducted by the EHT.

1. INTRODUCTION

Black holes are some of the most energetic and interesting objects in the universe. They exhibit immense gravity, which affects the geometry of the space-time environment in the vicinity of the black hole. These objects also possess an accretion disk or flow, which consists of material orbiting and spiraling into the black hole at extremely high velocities and temperatures. This environment creates high-energy plasma effects and bright emission that we can detect and observe. They also launch jets which influence the dynamics of their host galaxies. These conditions make these systems a prime location to study relativistic plasma physics and turbulence.

Several efforts have been made to study these objects in detail. The Event Horizon Telescope (EHT) collaboration has made a comprehensive observational effort to study M87*, a supermassive black hole at the center of the M87 galaxy located about 53 million light years from the Milky Way. The EHT observed a bright ring of emission which is consistent with the photon orbit around the system (K. Akiyama et al. 2019). The 2017 observations along one week observed a bright spot move from the east to the south, showing structural variability on event horizon scales. The subsequent observations over the next years have seen this variability change. The observations also show the change in the polarization structure in the image, which showcases the dynamics of the magnetic fields in the system (The Event Horizon Telescope Collaboration 2025).

In this study, we investigate the variability of the accretion flow of black holes through GRMHD simulations, giving us insights into dynamic process in the environment near these objects such as turbulence. In section 2, we find the correlation structure of a black hole simulation and define a functional form for the feature. By characterizing it, we reduce the variability to a few physically interpretable parameters and their velocities. In section 3, we measure these parameters from the simulations and then interpret their behavior over the spatiotemporal domain. Finally, we summarize results in section 4.

1.1. GRMHD

Accreting supermassive black holes exhibit complex, time dependent emission driven by a combination of relativistic gravitational effects, plasma physics, and magnetohydrodynamic turbulence. For sources observed by the Event Horizon Telescope (EHT), such as M87*, the dominant emission arises from the innermost regions of the accretion flow, where the plasma becomes hotter, more magnetized, and dynamically coupled to the curved spacetime of the Kerr metric (C. F. Gammie et al. 2003). To study the morphology and variability of this region, including the formation and evolution of spiral features, we rely on general relativistic magnetohydrodynamic (GRMHD) simulations.

GRMHD simulations solve the fluid dynamic equations of accreting plasma in the Kerr black hole spacetime and simulate emission and absorption to generate the images that would be seen by a distant observer. In

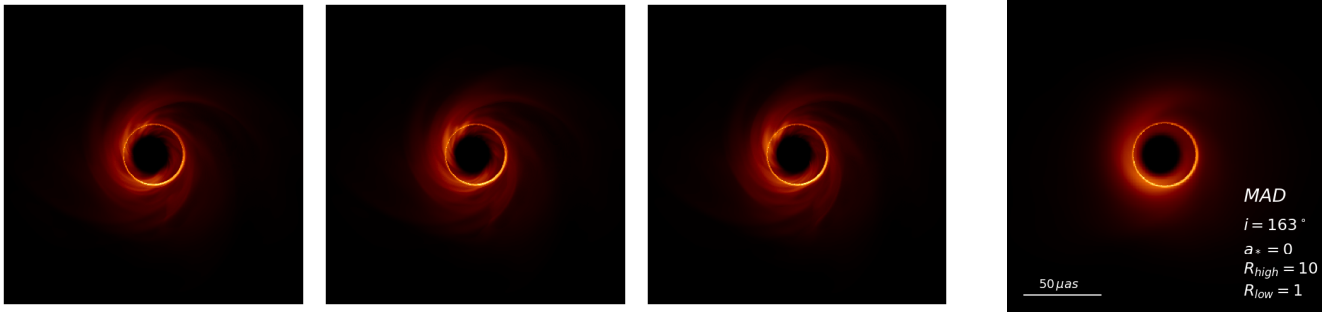


Figure 1. Snapshots of the black hole M87* simulated through GRMHD (in square root scale) for parameters: $R_{high} = 10$, $R_{low} = 1$, $a_* = 0$ (spin) and $i = 163^\circ$ (inclination). The first three panels represent the frames of the black hole at $5GM/c^3$ spacing. The final image is the average of 100 frames of the simulation. We can clearly see the parts of the accretion flow and the photon ring in the simulation.

these simulations, the fluid is treated as an ideal, single temperature fluid. There are several assumptions undertaken in the simulations. Firstly, we assume that the plasma can be treated as a fluid, although the mean free paths of particles in reality are often much longer than the length scales in the systems. Secondly, we assume that the plasma has infinite conductivity, such that the magnetic field lines are woven into the fluid. However, in actual accretion flows, due to kinetic processes, the fluid experience collisions which influence variability structures. These processes also affect the thermodynamics of the system. All of this effects may affect the variability in these system which are not captured by the simulations we used in this study (F. Foucart et al. 2016).

These simulations also include the strength and structure of the magnetic field in the surrounding environment, which determines the magnetic flux that threads the event horizon. Each of the simulations that are we are studying equilibrates into two accretion modes that are dependent on the magnetic flux. When the magnetic flux reaches a higher threshold value, the local magnetic pressure near the event horizon balances the inward fluid ram pressure, we obtain a magnetically arrested disk or a MAD state (A. Tchekhovskoy et al. 2011). In this state, the accretion flow is bumpy and there are several transient ejection events where magnetic flux bubbles that have accumulated on the horizon are expelled. This causes a shift from steady state accretion and results in thin, in-falling filaments. Contrary to this, when the magnetic flux at the horizon is much lower than the threshold value, the disk produces a standard and normal evolution or a SANE state (R. Narayan et al. 2012). This state has turbulent but well-ordered accretion, and magnetorotational instability (MRI) is the primary source for angular momentum transfer.

After solving the equations governing the GRMHD accretion flows, general relativistic radiative transfer (GRRT) is used to generate images. This process involves two steps: First, the photon trajectories are calculated backwards from the camera using the geodesic

equation. Then, the radiative transfer equation is solved along the computed photon trajectories. This process takes into account several parameters. They include the spin of the black hole (a^*), factors that describe the thermal electron landscape in the simulation (R_{high} and R_{low} ; M. Mościbrodzka et al. 2016) and the inclination angle of viewing (i). The spin and the inclination are photon ray parameters, while R_{high} and R_{low} are a particular model to paint on electron ion temperatures.

In GRMHD accretion flows, spiral structures emerge from conducting various analysis that involve variability. In D. Lee & C. F. Gammie (2021), the authors introduce a model for these spiral features using a Gaussian Random Field (GRF). However, their velocity and correlation structure simply prescribes the spiral arms. This motivates our work to create a theoretically motivated model for these features. Understanding the geometry of these spiral features such as the pitch angle, provides a direct probe to understanding variability in small scales.

GRMHD simulations also present the effects of strong gravitational lensing near the event horizon, which also affects the variability dynamics. Photons emitted from the innermost disk experience significant bending, and those orbiting near the unstable circular photon orbit contribute to a narrow, bright photon ring. Spiral features that approach the photon orbit are stretched, lensed, or partially wrapped around the black hole producing characteristic variability signatures near the photon ring.

For nearly face-on viewing angles, these spiral features become more easier to characterize, due to the azimuthal symmetries in the system. Hence, in this work, we use face-on (high inclination value) GRMHD-generated images to identify and characterize the spatiotemporal variability present in the accretion flows. By measuring various parameters such as the pitch angles of the resultant spiral variability structure as a function of radius and time, we obtain a quantitative description of the evolution of these variability structures in simulated accretion flows. This analysis allows us to directly relate image-domain variability, observable by the EHT,

to the underlying physical processes that govern accretion in the gravity regime.

In these study, the following GRMHD simulation parameters were used:

1. **Simulation:** Magnetically Arrested Disk (MAD)
2. **Spin (a_*):** 0
3. R_{high} : 10
4. R_{low} : 1
5. **Inclination (i):** 163°
6. **Time of Simulation:** $25,000 - 30,000 GM/c^3$
7. **Cadence:** $5 GM/c^3$

[Figure 1](#) shows the simulation for these parameters. This simulation is studied and analyzed in the rest of the paper.

2. METHODS OF THE PAPER

2.1. Quantifying the Variability

After analyzing the data from the GRMHD simulation for the specific parameters, we obtain movies of the black hole and the dynamics of the accretion flow around it. The frames in the movie contain information of the time series intensity of each pixel, given as $\xi(x, y, t)$, where ξ is the intensity as a function of the location of the pixel given by x and y on the frame and the time t , which can be interpreted as the frame number in the movie. The separation of the frames in the movie, or the time separation, is in black hole mass units or GM/c^3 . The spatial units are given by a half a microarcsecond (μas) per pixel.

To begin our analysis, we first computed the temporal Gaussian-smoothed mean of the image over a short timescale. We apply a Gaussian function across several frames (in the ‘time-direction’), which helps to quantify weights for each frame. In this process, each frame is weighted with this Gaussian function and divided by the integral of this function over the entire timescale (T). This expression is given by

$$\langle \xi \rangle(x, y, t) = \int \xi(x, y, t) \frac{1}{2\pi T} \exp \left[\frac{-(t - t_0)^2}{2T^2} \right] dt_0 \quad (1)$$

where, t is the time or frame number throughout the movie, t_0 is the center or reference frame of the movie and T is the timescale of the smoothed mean, which influences the width of the Gaussian. The integrals are sums of the Gaussian-weighted temporal slices.

In this case, we choose a small timescale of $T = 200$, to focus on small term variability and not consider long term variability and mass accretion effects, which is the dominant source as found by [B. Georgiev et al. \(2022\)](#). We will find that our variability structure emerges well-below the set timescale.

After finding this Gaussian-smoothed temporal mean, we subtract this mean ([Equation 1](#)) across the image to isolate the variability features in the image, which would help us better characterize them. This is represented by

$$I(x, y, t) = \xi(x, y, t) - \langle \xi \rangle(x, y, t) \quad (2)$$

To begin our variability analysis, we assess variability by comparing the mean subtracted intensity time series between neighboring or distant pixels within the same frame. We consider a frame in the GRMHD movie and set up a grid to characterize the spatial dimensions, locations, and geometry of the structure of features in the frame. We set our origin at the center of the black hole. We then define x_1 and y_1 , the location of the reference pixels and I_1 , the mean subtracted intensity at that point. We also define x_2 and y_2 , the locations of the other pixels to be correlated against the reference pixels and I_2 , the mean subtracted intensity at that location in Cartesian space. This helps us to spatially contextualize a given frame. Using this setup, the degree of variability between the mean subtracted intensity of the reference pixel (x_1, y_1) and the other pixels (x_2, y_2) is quantified using a normalized correlation based formulation that we laid out. It is given by

$$C(x_1, y_1, x_2, y_2, \Delta t) = \frac{\int I_1(t) I_2(t + \Delta t) dt}{\sqrt{\int I_1^2(t) dt \int I_2^2(t + \Delta t) dt}} \quad (3)$$

This equation can also be extended to polar coordinates by a coordinate transform from Cartesian to polar. In the polar case, r_1 and θ_1 will be the locations of the reference pixel and r_2 and θ_2 , will be the locations of the other pixels to be correlated with the reference pixels.

In [Equation 3](#), the normalization with intensity results in the correlation function that provides values between -1 and 1. A correlation of 1 indicates maximum correlation, while a correlation of 0 indicates complete non-correlation. On the other hand, a correlation of -1 indicates an anti-correlation between the pixels. Another important feature of this function is that it is invariant under switching of the spatial Cartesian coordinates.

$$C(x_1, y_1, x_2, y_2, \Delta t) = C(x_2, y_2, x_1, y_1, -\Delta t) \quad (4)$$

Similarly, in polar form, we can write,

$$C(r_1, \theta_1, r_2, \theta_2, \Delta t) = C(r_2, \theta_2, r_1, \theta_1, -\Delta t) \quad (5)$$

2.2. Applying this Formulation

In [Figure 2](#), we highlight an example of a selected reference pixel (r_1, θ_1) located approximately $30 \mu as$ to illustrate the temporal and spatial correlations using our correlation formulation described in [Equation 3](#), with respect to all pixels in the frame. We see that a clear spiral arm structure is formed, which depicts the variability structure across the spatial domain. In this case,

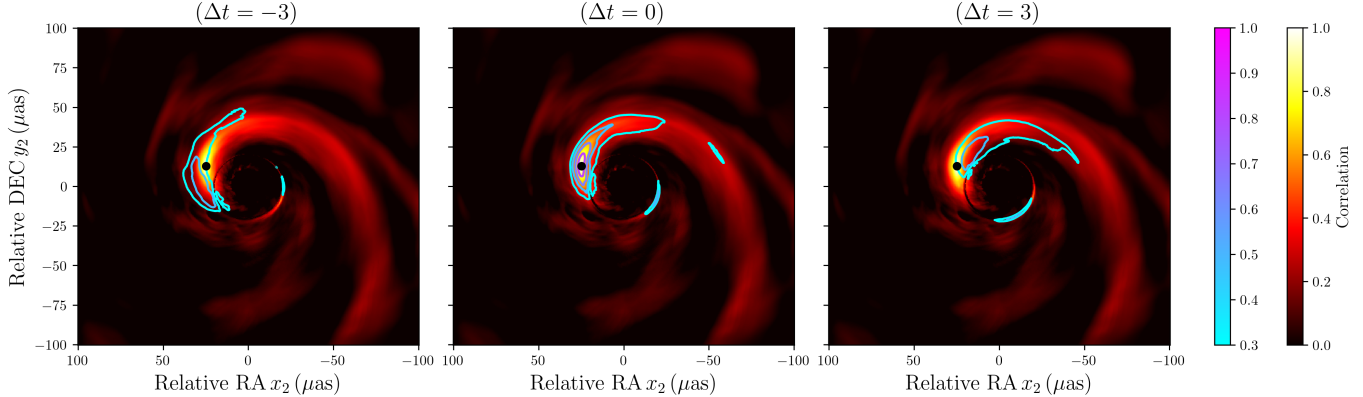


Figure 2. In this figure, we show the spatiotemporal variability structure after applying our correlation formulation described in subsection 2.1. We apply Equation 3 to entire pixels across the image with respect to the pixel marked by the black dot ($r_1 = 26$, $\theta_1 = -1.1$). The resultant spiral arm variability can be represented by $C(r_1 = 26, \theta_1 = -1.1, r_2, \theta_2, \Delta t)$. Across the three panels, the same hot colormap is applied, which represents the variability structure at $\Delta t = 0$. The contours, given by the cool colors, represent the variability structure at $\Delta t = -3$, $\Delta t = 0$, $\Delta t = 3$ and show the temporal evolution of the spiral arm. We can see that the maximum correlation is present at the reference pixel at $\Delta t = 0$. The maximum correlation shifts as a function of Δt , as seen in the contours. We can see that the spiral structure is moving outward counterclockwise as a function of Δt . We can also see a correlation signature at the photon ring on the other side of the black hole, which is a result of gravitational lensing.

the correlation is computed between the intensity time series of this reference pixel and those of all other pixels within a single frame. We observe that pixels in close spatial proximity to the selected pixel exhibit a higher degree of similarity. This correlation map unveils a distinct spiral arm-like variability structure, which becomes more diffuse when analyzed as a function of time lag, Δt . The chosen reference pixel is marked explicitly in the figure for clarity. As Δt increases, we can clearly trace the temporal evolution of this spiral variability pattern, highlighting how fluctuations propagate through the image domain over time. At the location of the reference pixel at $\Delta t = 0$, the value of the correlation is 1, due to normalization in Equation 3.

In Figure 2, we can also see a lensed feature of the variability structure near the photon ring, which represents the mapping of the structure due to the space-time curvature, which bends the light rays because of the black hole's immense gravity. In this work, we do not characterize the structure of the lensed feature as it is beyond the scope of this project, and we cut this feature out in our later analysis. Also, the GRMHD simulations that we considered in this study involve the use of fast light ray-tracing, which updates the fluid domain properties at every step of integration along the path of photons. This results in an improbable location of the lensed feature in this study. This work remains to be studied in the future.

2.3. Functional Form of the Spiral Arm

To assist in our characterization of the spiral structure represented in Figure 2, we perform a coordinate transformation in polar coordinates. In Figure 3, we can

see the structure in polar form corresponding to $\Delta t = 0$. The location of the special pixel is the same as before, $r_1 = 26$, $\theta_1 = -1.1$. This helps us to better visualize the correlation-based spiral arm structure surrounding the black hole. It enables us to analyze the azimuthal variation of the structure as a function of the radial distance from the black hole center. In the resulting polar representation, the spiral feature looks almost linear. However, around $50\text{ }\mu\text{as}$, a prominent kink becomes evident in the spiral pattern, which corresponds to a noticeable change in the pitch angle of the variability structure. After this kink, the spiral feature continues its linearity at a different slope. This distinct kink corresponds to the location where the spiral arm's geometry undergoes a transition that reinforces the presence of structural evolution within the variability pattern. We can also see that the spiral arm seems to go much further out in radius than inward.

To characterize the variability structure observed in the polar representation, we observe that a Gaussian is a poor approximation. The problem arises in the radial direction, where the correlation is determined by the ratio of the radii (r_1/r_2) and not by the difference ($r_1 - r_2$). The azimuthal direction is, however, simpler to fit, as it only requires three numbers - the correlation amount, the location of the peak and the width of the feature. We can see this in the third panel of Figure 3. Hence, we introduced a von-Mises model, or a wrapped Gaussian, to capture the underlying geometry of the correlation pattern along the azimuthal profile of the variability. We use a wrapped Gaussian as the model is a function of the azimuthal angle. In this model, we treat the correlation as a scaling factor. The model includes

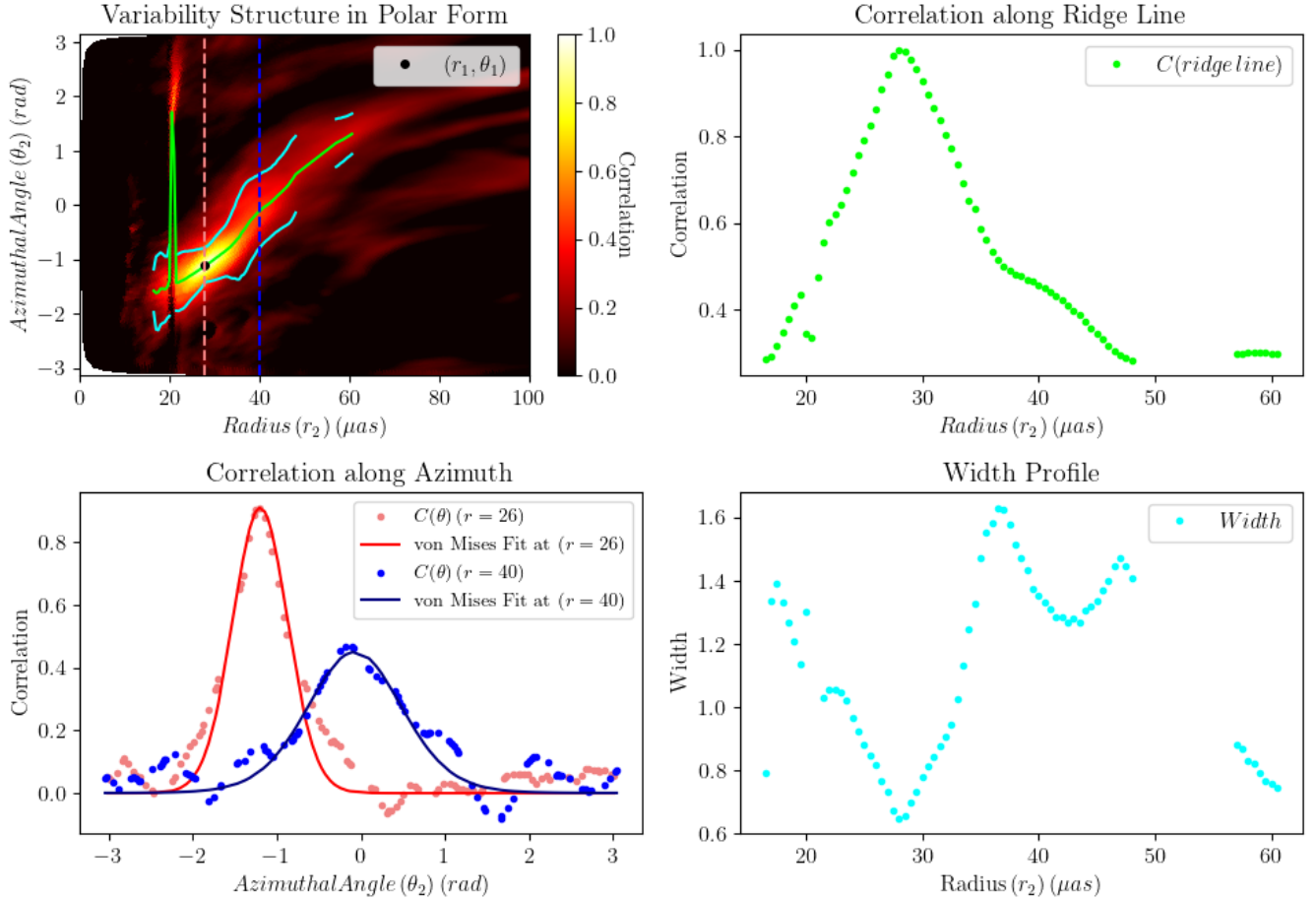


Figure 3. In this figure, we present our methods for the von-Mises fitting algorithm. In the first panel, we show a 2-D plot of variability structure for the $\Delta t = 0$ case from Figure 2, with the same reference pixels in polar form. We see that the spiral feature looks almost linear, with a kink at later radii. The green line represents the pitch angle (ψ) as a function of r_2 . The cyan lines represent the width parameter in the von-Mises model of the the variability structure described in Section 2.3. In the second plot we show the correlation profile along the lime ridge line described in the 2-D plot. We see that the correlation peaks at 1 at the reference pixel, due to the normalization in the correlation formulation. The dip in the correlation value around $r_2 = 20$ represents the lensed structure of the spiral variability structure. In the third plot, we show the correlation profile in the azimuthal direction at $r_2 = 26$ (the radius along the reference pixel location (r_1)) and $r_2 = 40$. We see that along the first radial line, the correlation peaks at one. In the other radial line, we see that the structure shifts, indicating a radial dependence in the correlation. In the fourth plot, we show the width profile of the feature. The cyan line in the plot represent the difference in the cyan lines in the first 2-D plot. We can see that the width of the feature is narrower near the reference pixels compared to other points. The gaps in the width profile represent the lensed structure. In this case, we show the width where the von-Mises fit was successful.

key parameters: the width of the variability feature (k), the pitch angle (ψ) and the maximum correlation (M) of the variability. The model is expressed as:

$$C(\theta, \Delta t) = M e^{k(\cos(\theta_1 - \theta_2 - \psi) - 1)} \quad (6)$$

Here, $C(\theta)$ denotes the modeled correlation value at azimuthal angle (θ). Here, parameters M , k and ψ depend on the location of the reference pixel (r_1), locations to the other pixels in the image (r_2) and the time lag (Δt). The definitions and variables used in this model are given in Table 1.

We can fit this von-Mises model for any reference pixel at a certain time lag ($r_1, \theta_1, \Delta t$). We first isolated the dominant variability feature and split up into 100 radial slices and fit the von-Mises model using a two-dimensional quasi-Newton optimization algorithm, specifically, the Broyden–Fletcher–Goldfarb–Shanno (BFGS) method (D. R. S. Saputro & P. Widyaningsih 2017) in each slice. The green line in Figure 3 represents the maximum correlation value found in each of the radial bins in the fit. We applied a cut (\tilde{c}) that filters correlation values below 0.2, to remove intrinsic noise in

the system. We applied then error bars (σ_{high} and σ_{low}) to our fits that reduce the likelihood of noisier points being included in the fit. This error bar formulation that we used is given by

$$e = \frac{C(\theta)(\sigma_{low} - \sigma_{high}) + \tilde{c}\sigma_{high} - \sigma_{small}}{\tilde{c} - 1} \quad (7)$$

where e is the error on the fit, σ_{high} is the higher error value and σ_{low} is the lower error value. We choose the error bar values to be $\sigma_{high} = 0.1$ and $\sigma_{low} = 0.0001$ such that points near $C = 1$ are fit exactly.

This fitting approach enables the investigation of the behavior of the von-Mises model parameters, the scaling factor or the maximum correlation M , the pitch angle ψ and the width parameter k across the image domain.

In reference to [Figure 3](#), $M(r_1, r_2, \Delta t)$ represents the maximum correlation of the feature and characterizes the correlation profile in the second plot of the figure. $\psi(r_1, r_2, \Delta t)$ represents the angle offset and characterizes the green ridge line shown in the 2-D plot. $k(r_1, r_2, \Delta t)$ is related to the difference in the cyan lines shown in the 2-D plot and characterizes the fourth plot in the figure.

These von-Mises parameters follow a flip symmetry, that is described by the following relations.

$$M(r_1, r_2, \Delta t) = M(r_2, r_1, \Delta t) \quad (8)$$

$$\psi(r_1, r_2, \Delta t) = -\psi(r_2, r_1, \Delta t) \quad (9)$$

$$k(r_1, r_2, \Delta t) = k(r_2, r_1, \Delta t) \quad (10)$$

Due to these properties, the von-Mises function follows the flip symmetry property described in [Equation 5](#). We can also see that when considering $\Delta t = 0$, $r_1 = r_2$ and $\theta_1 = \theta_2$, the correlation reduces to 1. This is expected due to the normalization in [Equation 3](#).

2.4. Applying von-Mises Formulation across Spatial Domain

To investigate the behavior of the von-Mises model parameters across the spatial image domain, we employ a systematic fitting procedure that spatially decomposes the GRMHD frame into 201 radial rings and 8 azimuthal slices, providing a structured grid for acquiring parameters. The initial angle ($\theta = 0^\circ$) of the azimuthal slices is located on the positive x-axis, considering the origin is at the center of the black hole. The azimuthal slices that we consider are located at angles from -180° to -135° in intervals of 45° . Now, along these radial bins and azimuthal slices, we choose our reference pixels (r_1, θ_1) where we find the degree of variability of the mean subtracted intensity of these pixels with respect to the entire image i.e all the other pixels in the frame (r_2, θ_2) . We consider each Δt frame separately. For each pixel within these radial and angular slices, we compute the correlation map using the [Equation 3](#). This step yields

a spatial correlation structure centered on the chosen pixel.

Hence, in this fitting method, we constrain our reference pixels as,

$$r_1 \in \{0, 0.5, 1, \dots, 100\},$$

$$\theta_1 \in \{-180^\circ, -135^\circ, -90^\circ, -45^\circ, 0^\circ, 45^\circ, 90^\circ, 135^\circ\}$$

We specifically chose this method of splitting up the frame into 8 slices, because we observe that the variability model is azimuthally symmetric across the spatial domain, meaning that the theta dependence should be the same. However, this is not true practically, hence for computational feasibility, we use θ_1 , the azimuthal coordinate for the reference pixels, to be from -180° to -135° in intervals of 45° .

After selecting the reference pixels, we apply the fitting procedure we laid out in [subsection 2.3](#). After applying this procedure for our selected pixels, we obtain values for the three von-Mises parameters $M(r_1, r_2, \Delta t)$, $\psi(r_1, r_2, \Delta t)$ and $k(r_1, r_2, \Delta t)$, which are described in [Table 1](#). In [Figure 4](#), the first row shows the 2-D plots of the correlation (C), the pitch angle (ψ) and the width parameter (k) in the spatial domain of the image. We can see a powerful signature for the correlation, the pitch angle and the width respectively, approximately along the diagonal of the domain. This shows that the location of the maximum correlation is around the regions of the pixels that are being referenced, i.e $r_1 = r_2$ (correlated to the whole image).

Hence, we can see that after the von-Mises fitting, we reduced our original 5-dimensional correlation function described in [Equation 3](#) to three 3-dimensional functions describing the parameters in [Table 1](#), which vary with r_1 , r_2 , and Δt .

2.5. von-Mises Parameter Characterization

To further investigate the properties of the von-Mises parameters in the spatial domain shown in [Figure 4](#), we define a geometric mean radius and the ratio of the radius to the pixels r_1/r_2 and apply them in the spatial domain. For the case of the pitch angle ψ , we define the logarithm of the ratio of the radius to the pixels $\log(r_1/r_2)$. We make this modification to preserve the invariant position (flip) symmetry in our model. These geometric mean radii are represented by the purple and lime lines in the 2-D plots of the parameters in [Figure 4](#). They are mathematically defined as

$$r_g = \sqrt{r_1 r_2} \quad (11)$$

We can see that the von-Mises parameters as a function of the geometric mean radius follow the flip symmetry described in [Equation 5](#). We can see this in,

$$M(\sqrt{r_1 r_2}, r_1/r_2, \Delta t) = M(\sqrt{r_2 r_1}, r_2/r_1, \Delta t) \quad (12)$$

$$\psi(\sqrt{r_1 r_2}, \log(r_1/r_2), \Delta t) = -\psi(\sqrt{r_2 r_1}, \log(r_2/r_1), \Delta t) \quad (13)$$

Table 1. Parameters used in the study and their significance to the each model.

von-Mises Parameter	Symbol	Physical Significance
Maximum Correlation	M	Maximum value in the variability structure
Width	k	Width of the variability structure
Pitch Angle	ψ	How spiral is the variability structure
Broken Power Law Parameter for M	Symbol	Physical Significance
Width	w_M	Half-width half maximum of the correlation
Sharpness	Δ_M	Smoothness of the peak correlation
Location	x_{0M}	Location of the maximum value of correlation
Height	f_M	Height of the maximum value of correlation
Broken Power Law Parameter for k	Symbol	Physical Significance
Width	w_k	Radial scale of the increase in width
Sharpness	Δ_k	Smoothness of the width peak
Location	x_{0k}	Location of the maximum value of width
Height	f_k	Value of the width of the feature
Linear Parameter	Symbol	Physical Significance
Slope	a	Angle offset of the feature (Pitch Angle)
Intercept	b	Azimuthal location of the maximum correlation

$$k(\sqrt{r_1 r_2}, r_1/r_2, \Delta t) = k(\sqrt{r_2 r_1}, r_2/r_1, \Delta t) \quad (14)$$

We investigated the structure of the relevant correlation signature across each geometric bin and decided to employ a broken power law fitting method to study the geometric properties of the correlation and the width parameter. This broken power law model is given by

$$\beta(\Delta, w) = \frac{\ln 2}{2\Delta \ln[\cosh(\frac{\ln w}{2\Delta})]} \quad (15)$$

$$C(x) = f \left(\frac{x}{x_0} \right)^\beta \left(\frac{1}{2} \left(1 + \left(\frac{x}{x_0} \right)^{1/\Delta} \right) \right)^{-2\Delta\beta}, \quad x = \frac{r_1}{r_2} \quad (16)$$

In these equations, w represents the half width half maximum of the broken power law, f is the scaling factor, x_0 represents the location of the peak, and Δ represents the sharpness of the peak. We use w in this model instead of β , because it is well constrained. Across a geometric mean radius, the broken power law follows a function of r_1/r_2 . In our analysis later, we investigate the trends of these four parameters. The parameters are described in [Table 1](#). A typical broken power law, however, has a rising and falling power law, but to preserve the flip property, we set them to be the same, β . In this model, we also need the non-standard parameter, the sharpness (Δ), because the fits later fail, if this parameter is not included. In this model, to preserve the flip symmetry described in [Equation 4](#), we apply the broken power law model to the correlation and the width as a function of r_1/r_2 across each geometric mean radii bin. In this formulation, we can also see that when $x = x_0 = 1$ and $f = 1$, the function reduces to 1, satisfying the condition we set when normalizing.

For the case of the pitch angle, after investigating the geometric mean radii bins, we decided to employ a simple linear fit. This model is given by

$$\psi(x) = a(r_g, \Delta t) \log\left(\frac{r_1}{r_2}\right) + b(r_g, \Delta t) \quad (17)$$

In this model, a represents the slope and b represents the intercept. In this case, we apply the line model to the pitch angle as a function of $\log(r_1/r_2)$ across each geometric radial bin, to preserve the flip property described in [Equation 5](#). In this case, when we consider the flip property, we obtain a change in the sign for the pitch angle because of the logarithm of the ratio.

This can be given by

$$\psi(r_1, r_2, \Delta t) = -\psi(r_1, r_2, -\Delta t) \quad (18)$$

Due to this special relation, we obtain the following properties for the slope and the intercept,

$$a(r_g, \Delta t) = a(r_g, -\Delta t) \quad (19)$$

$$b(r_g, \Delta t) = -b(r_g, -\Delta t) \quad (20)$$

We will see this property in our results analysis.

To begin fitting for our parameters of broken power law and linear parameters, we used an edge finding algorithm to constrain our fitting near the diagonal (in the 2-D plot of [Figure 4](#)) where the parameter signatures are relevant. This edge finding algorithm also cuts out the lensed feature in the frames and prevents the propagation of bad fits when there are multiple spiral arms in the domain. We also use a peak-finding algorithm to filter out profiles that exhibit multiple peaks. This is to prevent fitting super noisy data. To

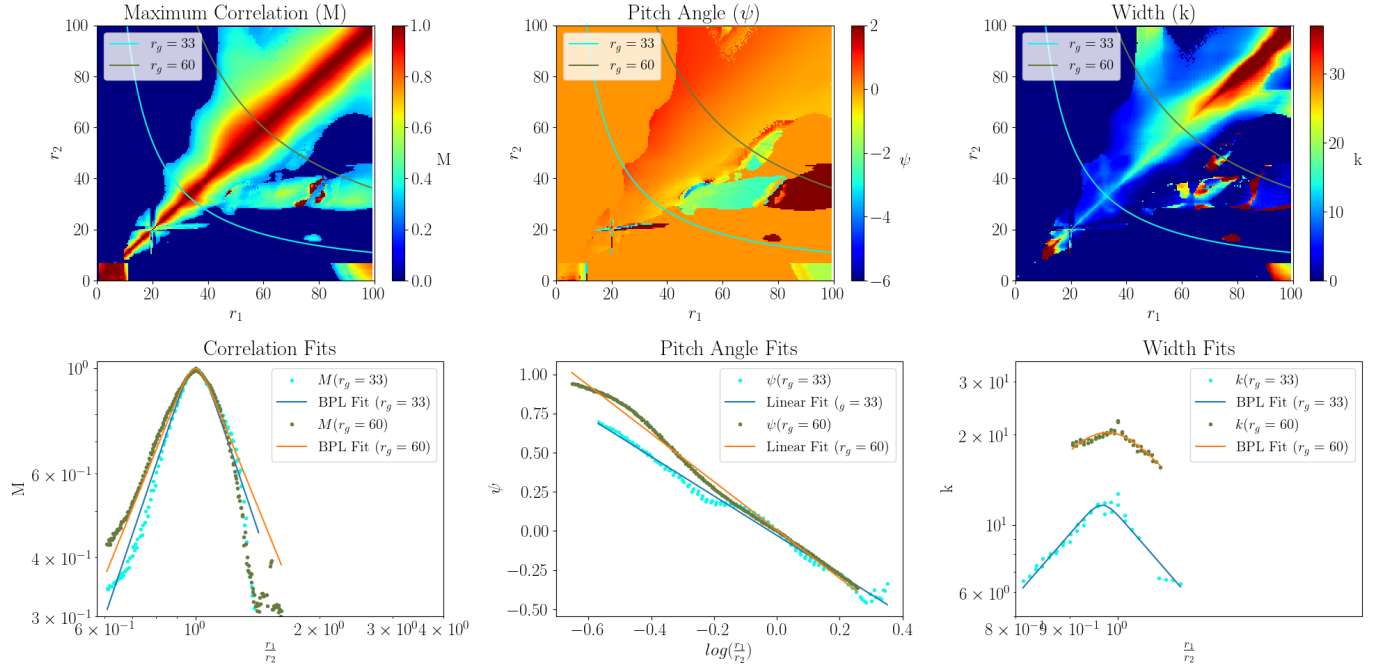


Figure 4. In this figure, we show the behavior of the von-Mises parameters at $\Delta t = 0$ and for the azimuthal slice $\theta_1 = 0^\circ$. In the first row, we show the 2-D plots of the three parameters as a function of r_1 , the reference pixels and r_2 , the other pixels in the image. We can see that the maximum parameter values are higher near the diagonal, indicating that the maximum correlation occurs near the reference pixel for $\Delta t = 0$, which is where $r_1 = r_2$. We also plot the lines of constant geometric radius in blue and dark green, described in Equation 11. In the second row, we plot the parameter profiles of the von-Mises parameters respectively, along these lines, corresponding to their colors in the second and third plot. We also show our corresponding broken power law and linear models. We can see that the broken power law and linear models are sufficient to describe the observed behavior, as we can see that the peak correlation fit occurs at 1, the slope of the pitch angle and the value of the width change as a function of the geometric mean radius.

employ the fits, we used our two-dimensional quasi-Newton optimization algorithm, specifically, the Broyden–Fletcher–Goldfarb–Shanno (BFGS) method again (D. R. S. Saputro & P. Widyaningsih 2017).

In Figure 4, the second row shows the structure and the fits across the profiles of the von-Mises model parameters at different geometric mean radii ($r_g = \sqrt{r_1 r_2}$). We can clearly see that the broken power law fits for the correlation and the width, and the linear fits for the pitch angle.

We also carried out the same set of methods to parameterize the spatial characteristics of the spiral arm for the case of $\Delta t = 0, 1, 2, 3$, which corresponds to $\Delta t = 5, 10, 15, 20 GM/c^3$ to investigate the change in the parameters of the variability structure in the temporal domain.

3. RESULTS

3.1. Variation of Parameters in Spatiotemporal Domain

After applying our set of methods to quantify the spatial geometry of the variability structure, we investigate the behavior of the broken power law parameters (M and k) and the linear parameters (ψ) of the von

Mises model, as a function of the geometric mean radii ($r_g = \sqrt{r_1 r_2}$) we defined in the previous section. This investigation provides us with a clear geometric profile of the variability structure across the spatial domain. We also investigate the behavior of the parameters for the $\Delta t = 3$ case, giving us insights of the temporal behavior of the structure.

1. Correlation ($M(r_1, r_2, \Delta t)$) Fits: In the first row Figure 5 we express the profiles of the width (w_M), sharpness (Δ_M), the location of the peak (x_{0M}) and the height (or scaling factor f_M) of the correlation broken power law model at $\Delta t = 0, 1, 2, 3$. We averaged across each azimuthal slice (azimuthal location of the reference pixels) that we consider during our von-Mises fitting since the feature is azimuthally symmetric. In these plots, at $\Delta t = 0$ we can see that the location and the height of the peak is constant at 1, this is due to normalization property of the correlation function. We can also see the variation of width across the spatial domain. The sharpness does not indicate a clear pattern, as it is a non-standard parameter that helps to obtain a broken power law model. Across the Δt values, we see that the width stays

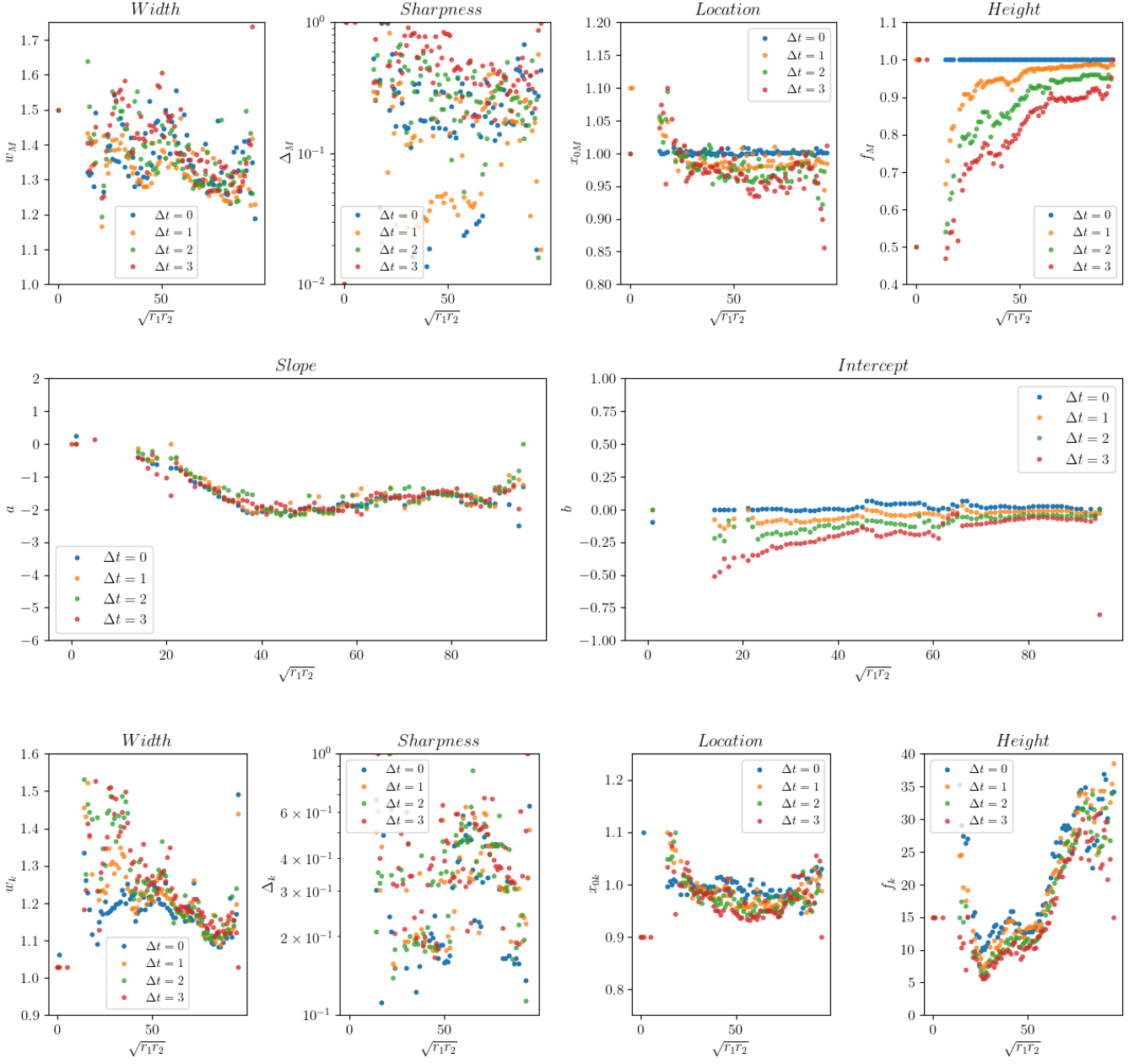


Figure 5. In the first row, we show the azimuthally averaged profiles for the broken power law parameters of the von-Mises correlation (M). We show the profiles for the width (w), sharpness of the peak (Δ), location of the peak (x_0) and the height of the peak (f) as a function of the geometric mean radius at $\Delta t = 0, 1, 2, 3 GM/c^3$ with blue, orange, green and red respectively. In the second row, we show the linear model parameters of the von-Mises pitch angle (ψ). We show the profiles for the slope (a) and the intercept (b) as a function of the geometric mean radius at $\Delta t = 0, 1, 2, 3$ with the same color coding as before. In the third row, we show the broken power law parameters of the von-Mises width (k). We show the profiles for the width (w), sharpness of the peak (Δ), location of the peak (x_0) and the height of the peak (f) as a function of the geometric mean radius at $\Delta t = 0, 1, 2, 3$. The physical significance of the parameters are described in Table 1.

around 1.3. We see a shift of values in sharpness (Δ), indicating that the correlation peaks become smoother. The position of the peak also changes slightly, indicating a change in the maximum correlation along the reference pixels (r_1, θ_1). We see

that the peaks move outward, as seen in Figure 2. This provides us with a measure of the radial velocity of the feature, which we will investigate in the future. We can also see that the peak correlation (f) decreases, indicating a loss of correlation

and the feature getting more diffuse, with material closer to the horizon diffusing faster.

- 2. Pitch Angle ($\psi(r_1, r_2, \Delta t)$) Fits:** In the second row of [Figure 5](#), we express the slope (a) and the intercept (b) profiles of the pitch angle (ψ) for $\Delta t = 0, 1, 2, 3$. We averaged across each azimuthal slice (azimuthal location of the reference pixels) that we consider during our von-Mises fitting since the feature is azimuthally symmetric. At $\Delta t = 0$, we see that the slope becomes more negative as a function of the geometric mean radii and exhibits a distinct kink at a certain radius, after which the slope increases. This indicates that the spiral variability structure is not a constant spiral throughout the spatial domain. In the intercept plot, we see that the averaged intercept stays constant around 0, which is expected because the value equals the azimuthal slice position across the spatial domain. Across Δt , we see that the slope stays constant and the distinct kink is preserved. In the second plot, we see that the averaged intercept is shifting faster near the black hole, indicating a rotation. This rotation is about 0.03 radians per GM/c^3 .
- 3. Width ($k(r_1, r_2, \Delta t)$) Fits:** In the third row of [Figure 5](#), we express the profiles of width (w_k), sharpness (Δ_k), location of the peak(x_{0k}) and the height (or scaling factor f_k) of the von-Mises width (k) broken power law at $\Delta t = 0, 1, 2, 3$. We averaged across each azimuthal slice (azimuthal location of the reference pixels) that we consider during our von-Mises fitting since the feature is azimuthally symmetric. At $\Delta t = 0$, we see that the width, which represents the kink of the von-Mises width (represented by the slope cyan lines in the 2-D plot in [Figure 2](#)), was measured to be about 1.2 which indicates that there is a population of spiral arms, each with a slightly different pitch angle. The dependence of w_k on radius will be investigated in future work. There is no clear spatial trend in the delta parameter. For the location of the peak correlation (x_0), we see that it is roughly located at 1, which is expected. We see a decreasing and then increasing behavior for the peak width height, which indicates fatter spiral features further out and thin spiral features close in. Across Δt , we see that the kink of the width increases slightly at lower radii, which suggests that the spiral arms become diffuse. We also see that there is no clear temporal trend in the delta parameter and the peak width. The position of the peak (x_0) also changes by a tiny amount, but overall remains constant.

In [Figure 5](#), we see that parameter trends are becoming noisier at geometric mean radii closer to 20 μ as. This

can be attributed to the presence of a photon ring at that radius. Also, along the photon ring, we also see lensing features of the variability structure, which also influence noisy features at that radius.

3.2. Discussion and Analysis

In the previous section, we laid out the results that we obtained through our variability analysis. We can see several interesting findings, such as the kink in the pitch angle and the trend in the width of the von-Mises width parameter k .

The kink in the slope is suggestive of change in the flow dynamics of GRMHD. The innermost part of the accretion flow is subject to an in-fall of material towards the horizon due to general relativistic effects, compared to the outer sections of the accretion disk. This kink in the value might the transition point in these accretion dynamics. It might also be suggestive of a lensing effect. More investigation and future work is required to study the cause for this effect.

Looking at the trend for the width parameter w of the von-Mises width k , we can see that there might be a population of spiral arms that influence the dynamics of the variability structure.

Analyzing these results, we can also make a rough measurement of the radial and azimuthal velocity of the structure. By looking at the position of the peak for the correlation M , we can see that the variability structure is in-falling, due to the values of x_0 getting smaller faster near the black hole as a function of Δt . We can also look at the plot for the intercept of the pitch angle ψ where we see that the averaged intercept is shifting faster near the black hole, indicating a rotation. This rotation is roughly about 0.03 radians per GM/c^3 . This requires more future work.

4. CONCLUSION

In this work, we introduced a new image-domain framework for characterizing the geometry and evolution of spiral arm variability structures in GRMHD simulations of black hole accretion flows. By formulating a normalized correlation function that operates in the spatiotemporal domain, we were able to characterize the variability structures within turbulent accretion flow images and track how these structures propagate and diffuse as a function of time lag (Δt). This correlation formalism reveals a clear spiral variability feature centered on any chosen reference pixel and recovers the expected signature of gravitational lensing near the photon ring.

Using this correlation map as a basis, we transformed the variability structure to polar coordinates and developed a ridge-finding procedure that traces the spine of the spiral arm across radii. Modeling the azimuthal profile of this ridge with a von-Mises functional form allows us to extract three key parameters that describe the geometry of the structure: the maximum variability amplitude or the correlation (M), the pitch angle (ψ),

and the feature width (k). By fitting these parameters across 201 radial bins and 8 azimuthal slices and further decomposing their radial dependence through geometric mean radii to preserve symmetries, we produced a comprehensive parameterization of the spiral variability structure.

The von-Mises parameters show physically interpretable behavior. The correlation amplitude and width follow a broken power-law dependence on radius which is consistent with a transition from tight correlations in the inner-disk variability to more diffuse outer-disk structures. The pitch angle shows a distinct kink at a geometric mean radius, indicating a change in the dynamical regime of the flow, potentially related to a shift in shear rate, turbulence, or changes in the local inflow speed. Comparing the $\Delta t = 0, 1, 2, 3$ cases reveals that the variability structure becomes wider, smoother, and increasingly displaced in the temporal sense, allowing us to infer the effective propagation velocity and diffusion of the spiral arm. These trends are consistent even after azimuthal averaging and are robust to the presence of strong lensing features near the photon ring, which introduce additional noise at radii near $r_g = 20 \mu\text{as}$.

Together, these results demonstrate that spiral arm variability in GRMHD simulations is a characterizable, measurable, and parametrically describable structure whose geometry evolves spatiotemporally. Our model captures this complexity in a set of parameters and

provides an image-domain method to geometrically describe these structures. Specifically, we can use the 10 described parameters and their temporal parameters to distinguish which simulations are consistent with observational data in an interpretable way. We can measure them from the data and simulations and discriminate between simulations.

Beyond its importance for understanding accretion physics, this framework provides a pathway for improving the Gaussian Random Field (GRF) variability models currently used in EHT analyses. By enabling the subtraction of structured, non-Gaussian variability directly from simulation images, our model can help separate turbulent fluctuations from features of interest in respective studies, improve interpretation of EHT reconstructions, and enhance future imaging pipelines. As the EHT prepares for its upcoming movie campaign, the parameterized variability model developed here offers a powerful tool for linking image-domain variability to observable relativistic plasma dynamics and may serve as a foundation for comparisons between theory and observations.

ACKNOWLEDGMENTS

I thank Dr. Boris Georgiev, Dr. Chi-kwan Chan, University of Arizona and Steward Observatory faculties for their invaluable contribution to the development of this project.

REFERENCES

- Akiyama, K., Alberdi, A., Alef, W., et al. 2019, *The Astrophysical Journal Letters*, 875, L1, doi: [10.3847/2041-8213/ab0ec7](https://doi.org/10.3847/2041-8213/ab0ec7)
- Foucart, F., Chandra, M., Gammie, C. F., & Quataert, E. 2016, *MNRAS*, 456, 1332, doi: [10.1093/mnras/stv2687](https://doi.org/10.1093/mnras/stv2687)
- Gammie, C. F., McKinney, J. C., & Tóth, G. 2003, *ApJ*, 589, 444, doi: [10.1086/374594](https://doi.org/10.1086/374594)
- Georgiev, B., Pesce, D. W., Broderick, A. E., et al. 2022, *ApJL*, 930, L20, doi: [10.3847/2041-8213/ac65eb](https://doi.org/10.3847/2041-8213/ac65eb)
- Lee, D., & Gammie, C. F. 2021, *ApJ*, 906, 39, doi: [10.3847/1538-4357/abc8f3](https://doi.org/10.3847/1538-4357/abc8f3)
- Mościbrodzka, M., Falcke, H., & Shiokawa, H. 2016, *A&A*, 586, A38, doi: [10.1051/0004-6361/201526630](https://doi.org/10.1051/0004-6361/201526630)
- Narayan, R., Sadowski, A., Penna, R. F., & Kulkarni, A. K. 2012, *MNRAS*, 426, 3241, doi: [10.1111/j.1365-2966.2012.22002.x](https://doi.org/10.1111/j.1365-2966.2012.22002.x)
- Saputro, D. R. S., & Widyaningsih, P. 2017, in *American Institute of Physics Conference Series*, Vol. 1868, The 4th International Conference on Research, Implementation, and Education of Mathematics and Science (4th ICRIEMS): Research and Education for Developing Scientific Attitude in Sciences And Mathematics (AIP), 040009, doi: [10.1063/1.4995124](https://doi.org/10.1063/1.4995124)
- Tchekhovskoy, A., Narayan, R., & McKinney, J. C. 2011, *MNRAS*, 418, L79, doi: [10.1111/j.1745-3933.2011.01147.x](https://doi.org/10.1111/j.1745-3933.2011.01147.x)
- The Event Horizon Telescope Collaboration. 2025, arXiv e-prints, arXiv:2509.24593, doi: [10.48550/arXiv.2509.24593](https://doi.org/10.48550/arXiv.2509.24593)